Planetary Geology with Imaging Radar: Insights from Earth-based Lunar Studies, 2001–2015

Bruce A. Campbell
Center for Earth and Planetary Studies, Smithsonian Institution, MRC 315, P.O. Box 37012, Washington, DC 20013-7012, USA
Received 2015 October 2; accepted 2016 January 4; published 2016 May 5

Abstract

Radar exploration of the Solar System changed dramatically during and beyond the period of the *Magellan* mission to Venus. These changes included an expansion of the community familiar with microwave data, and the forging of a strong connection with polarimetric scattering models developed through terrestrial field measurements and airborne radar studies. During the period, advances in computing power and imaging techniques also allowed Earth-based radar experiments to acquire data at the highest spatial resolutions permitted by their transmitter systems. This paper traces these developments through a case study of lunar observations over the past 15 years, and their implications for ongoing and future Solar System radar studies.

Key words: Moon – planets and satellites: surfaces

Online material: color figures

1. Introduction

The scientific study of the planets, satellites, and small bodies of the Solar System relies to a large degree on remote sensing in wavelengths across the electromagnetic spectrum. Even for the Moon, where landed missions have occurred a number of times, orbital and Earth-based remote observations remain an important part of geologic investigations, landing site selection, and resource or hazard assessment. In these studies, active microwave (radar) techniques have played a significant role, often filling gaps in our understanding of surface and subsurface physical properties that cannot be addressed by, for example, visible imaging or infrared spectroscopy (Ostro 1987; Neish & Carter 2014). As with other remote sensing methods, the use of radar data has progressed through the constructive interplay of improved instrument and processing capabilities and the development of theoretical models and empirical evidence needed to translate an arcane suite of signals into useful geophysical descriptions of the target.

Radar uses an actively transmitted signal with a sensitive receiving system to obtain information about targets at a distance. The signal itself has, to degrees that vary with the equipment and the experiment, a controlled pulse length, frequency range, polarization, and incident geometry at the location of interest. The receiving system in turn may filter the signal in time-delay and frequency, measure different polarizations, and have a different geometry with respect to the target. One of the great advantages of radar sensors for geologic studies of the planets is the penetration depth of the signals. Where optical, infrared, and thermal infrared measurements respond to the properties of the upper few microns to centimeters, radar signals can probe meters to kilometers below the surface depending upon the composition of the target material and the choice of wavelength.

From 1964 to the late 1980s, Earth-based radar revolutionized our understanding of planetary motions and distances, provided the first hints of the unique properties of the icy outer planet satellites (Ostro et al. 1992), mapped the Moon in support of *Apollo* (Thompson & Dyce 1966; Pettengill & Thompson 1968; Thompson et al. 1970; Thompson 1974, 1987; Zisk et al. 1974), and paved the way (Campbell et al. 1972, 1989) to orbital radar mapping of Venus by the *Pioneer-Venus*, *Venera 15/16*, and *Magellan* missions (Saunders et al. 1992; Butrica 1996). Analysis of the global dataset collected by *Magellan* greatly enlarged the community within planetary science familiar with the interpretation of radar measurements, and motivated studies to understand the relationship between echo properties and natural surface roughness.

Efforts to understand radar reflections from unfamiliar settings spawned some of the earliest modeling of electromagnetic scattering from natural surfaces (e.g., Hagfors 1964; Hagfors & Evans 1968). Planetary observations helped to pioneer the study of radar polarization characteristics as a guide to surface properties, and the *Magellan* era coincided with a tremendous increase in airborne radar capability that would make "imaging polarimetry" a widely used technique in soil science, forestry, and geology (Evans et al. 1986; van Zyl et al. 1987). The synergy between planetary investigations and terrestrial airborne and field studies that emerged in this period, coupled with greatly improved image spatial resolution from

Earth-based and orbital sensors, has significantly contributed to making lunar and planetary radar remote sensing a quantitative technique.

In this article, we review the progress of planetary radar through a case study of the past 15 years of Earth-based mapping of the Moon. Over the period since *Magellan*, the radar science community has combined synthetic aperture processing techniques and our growing understanding of surface roughness statistics and scattering properties to address a broad range of scientific questions. The methods demonstrated in lunar work (where some degree of "ground truth" exists) in turn benefit radar studies of Mercury, Venus, Mars, the asteroids, and the icy outer planet satellites. Section 2 provides an outline of Earth-based planetary radar mapping techniques. Section 3 highlights the importance of radar polarization characteristics to the understanding of surface or subsurface physical properties, Section 4 describes the characterization of natural surface roughness (small-scale topography) relevant to radar scattering, and Section 5 reviews models for radar penetration and loss in planetary surface materials like ices or the lunar regolith. Sections 6 and 7 offer a survey of lunar imaging radar observational and scientific work over the past fifteen years. Section 8 summarizes these results in the context of other planetary radar work, and discusses future directions in the field.

2. Earth-based Radar Mapping

The steps involved in creating radar images of the Moon or planets from Earth-based observatories parallel those used in airborne and spaceborne synthetic aperture radar (SAR) systems (e.g., Cumming & Wong 2004). Earth-based radar observations discussed here are conducted using transmitters at the Arecibo Observatory (12.6 and 70 cm wavelength), but similar observations can be made with the Goldstone Solar System Radar (3.5 cm wavelength; e.g., Margot et al. 1999, 2000), often in conjunction with receivers at the Green Bank Telescope. Key to any measurement is a prediction for the varying time delay and Doppler shift between the transmitter and a chosen point on the planet's surface. These ephemerides are used to adjust the inter-pulse timing and phase of either the transmitted or received signal so that this target point appears at a known delay and frequency shift after basic processing. Signals arriving at the receiver are mixed to baseband and low-pass filtered (to limit the noise bandwidth) prior to analog-to-digital (A/D) conversion.

Radar observations measure the round-trip delay between transmitter and receiver, with a time resolution that is related to the effective length of the transmitted pulse. A system may transmit a monochromatic signal with a nominal square pulse of duration τ, but this limits the power that arrives at the target. Fine time resolution and much higher average signal power can be achieved by transmitting a signal whose frequency or phase
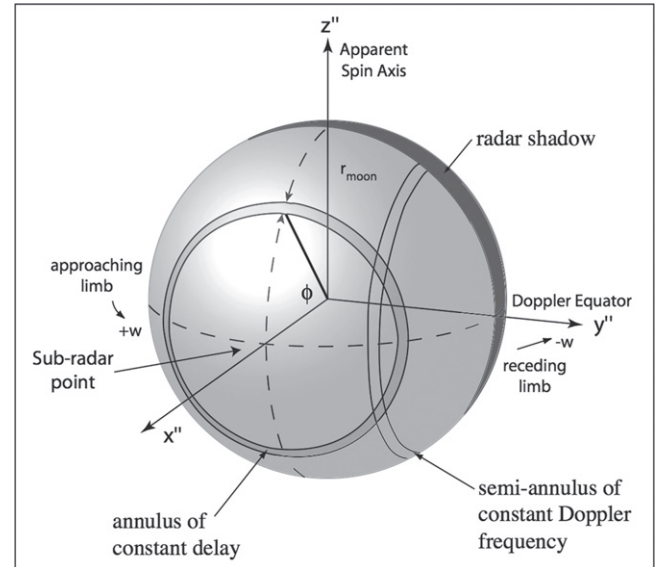

Figure 1. Geometry of delay-Doppler imaging. The sub-radar point is where the line between the planet's center of mass and the sensor intersects the surface. Greater distance from the sub-radar point along the x'' axis corresponds to annuli, with constant incidence angle ϕ, of greater time delay in the radar echo. The vertical axis, z'', is the apparent spin axis, and increasing distance along the y'' axis corresponds to greater Doppler shift. Adapted from Stacy (1993).

varies in a deterministic way over a longer period. The reflected signal is correlated with this phase or frequency signature, allowing for "pulse compression" to a value of $\tau = 1/\mathrm{BW}$, where BW is the range of frequencies in the linear frequency-modulated "chirp," or to the time interval (baud) between alternating phase values in a pseudo-random noise (PN) or Barker code imposed on a monochromatic signal (Evans 1968). Application of pulse-compression methods, along with low-pass filtering to exclude noise components outside of the desired frequency range for the target, provide much of the leverage in overcoming the strong (inverse fourth power) dependence of radar echo power on distance.

Perhaps the most far-reaching of methodologies developed during the early period of planetary radar was delay-Doppler imaging (Hagfors & Evans 1968). Sharing similarities with SAR techniques developed for airborne imaging sensors in the 1950s, this method forms a coordinate system from the basic time-delay resolution of the radar (the x'' axis in Figure 1) and the Doppler shift in frequency (the y'' axis in Figure 1) of echo components as the sensor and target move with respect to each other.

The horizontal resolution of the radar image along the time-delay axis is the projection of the pulse length onto the surface of a reference sphere. In terms of the radar incidence angle (the angle between the illuminating ray and the normal to the
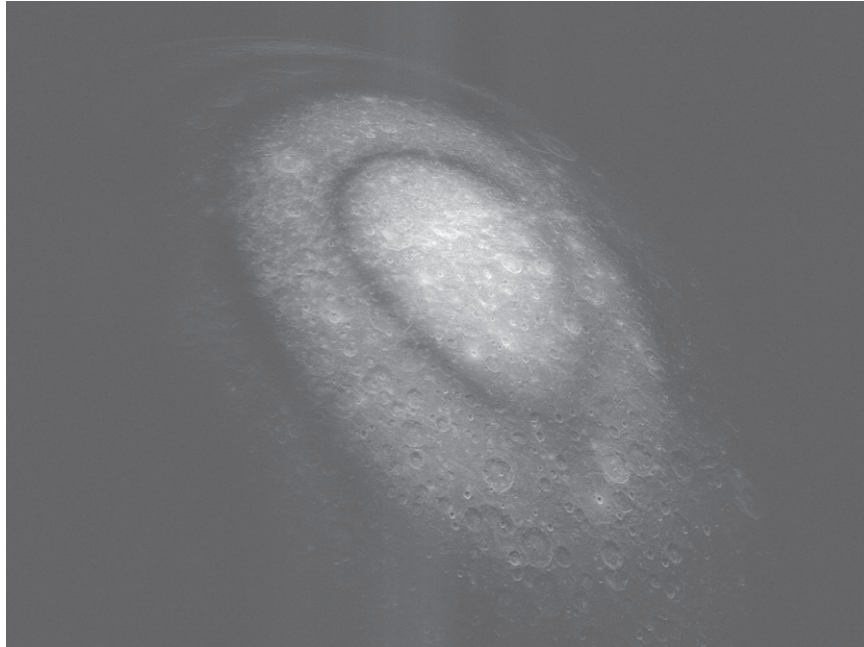
Figure 2. A delay-Doppler image of the southern highlands on the Moon at a radar wavelength of 12.6 cm. Time delay is along the vertical axis, and Doppler frequency shift is along the horizontal axis. The dark rings are the nulls of the beam pattern of the Arecibo antenna.

surface), ϕ, the "range resolution," Δr, is:

$$\Delta r = \frac{c\tau}{2\sin\phi} \qquad (1)$$

where c is the speed of light in the atmosphere or vacuum next to the surface. Spatial resolution along the Doppler frequency axis varies with angular distance from the direction of apparent spin, with areas at greater angular offset having coarser horizontal footprints (i.e., greater blurring) for any given change in frequency. An interesting aspect of this type of imaging is that the spatial resolution is independent of the range to the target—only the strong drop in echo power with target range limits the practical application to more distant objects.

With the echoes sorted into linear arrays corresponding to equal delay time, a Fourier-transform yields resolution cells whose horizontal scale on the surface is related to the limb-to-limb frequency range (i.e., the apparent spin rate) of the target and the inverse of the duration, T_c, over which coherent signals are obtained. The resulting coordinates of time and Doppler shift (often called "azimuth" from the terminology of airborne systems) (Figure 2) can be re-mapped to latitude and longitude based on the relative positions and motions of the observer and target (cf. Campbell et al. 2007).

As initially developed, Earth-based delay-Doppler techniques are based on a subset of the complete approach to SAR image formation. The best possible delay resolution is realized by the pulse compression, but basic Doppler processing will not yield arbitrarily fine resolution along the azimuth axis due

to migration of a point on the ground in both range (delay) and range-rate or Doppler frequency over the coherence interval (Cumming & Wong 2004). In order to achieve the fine spatial resolution allowed by long coherence intervals, it is necessary to apply "focusing" to the delay-Doppler array (e.g., Stacy 1993). At present, this added level of complexity is only required in lunar observations, since signal-to-noise ratio constraints prevent higher-resolution imaging of most other bodies.

SAR processing resamples (or interpolates) the echo information for a desired point on the target to compensate for the change in range over time. For an airborne platform, this is often a predictable function of the along-track motion, but over large illuminated regions on the Moon the range migration can vary significantly. It is thus applied based on predictions of lunar motion for a small region around a particular location. A second step then applies a time-varying phase to the data that corrects for the change in apparent Doppler frequency of the area during the observation, and the resulting focused patches are assembled into a complete map (Figure 3; Campbell et al. 2007, 2010).

Multiple independent maps are summed to reduce speckle, an unavoidable source of multiplicative variation in coherent imaging, and the echoes in each polarization are further normalized to the background system noise power. Delay-Doppler imaging cannot distinguish between echoes that arise from sites in the northern and southern hemispheres of a sphere (or the corresponding locus of points on an irregular object)
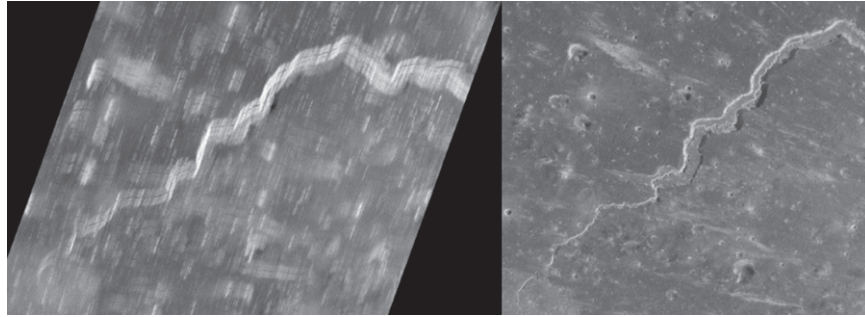
Figure 3. An unfocused 12.6 cm radar image of a sinuous rille on the Aristarchus Plateau (left), and the same data after focusing and mapping to latitude–longitude coordinates (right). Motion of the target region over the coherence interval of an observation leads to substantial smearing along the Doppler-frequency axis that must be compensated with a time-dependent phase variation.
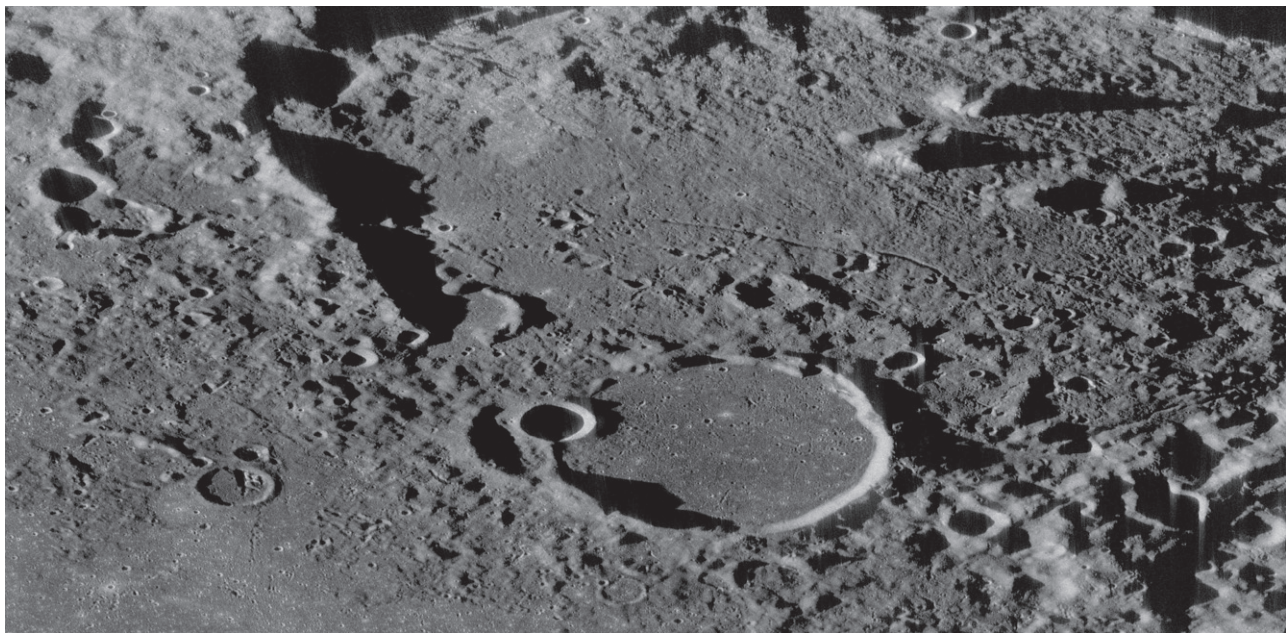

Figure 4. Long radar shadows cast by lunar topography in northeastern Humboldtianum basin. The illumination direction is from lower left. The 58 km diameter crater Bel'kovich-A is at lower center.

with identical time and frequency properties. This "north-south" ambiguity can be almost completely avoided with judicious pointing of the transmitted antenna beam (Figure 2) in studies of the Moon, but imaging of more distant bodies such as Venus or Mars must deal with the overlap of echoes from the two hemispheres.

As with observations made using solar illumination, the radar images have shadows cast by topography, and these shadows lengthen as the illumination becomes more oblique near the limbs or poles (Figure 4). Radar observations also exhibit a foreshortening or parallax behavior along the time-delay axis, since the echoes from elevated terrain will arrive earlier than those of a point at the same geographic position on a reference spheroid. When the radar incidence angle matches the slope angle of the terrain, this foreshortening is called layover, and essentially compresses the resolution cells along the slope into a single delay location. The away-facing side of the topography (such as a ridge) is imaged, but is much elongated in the map projection.

3. Polarimetry

The polarization state of a reflected radar signal contains significant information about the physical characteristics of the target region. The polarization of an arbitrary signal is represented by the four-element Stokes vector, here given for

the orthogonal circular modes:

$$\begin{vmatrix} S_1 \\ S_2 \\ S_3 \\ S_4 \end{vmatrix} = \begin{vmatrix} \langle A_L^2 \rangle + \langle A_R^2 \rangle \\ 2\langle A_L A_R \cos \delta \rangle \\ 2\langle A_L A_R \sin \delta \rangle \\ \langle A_L^2 \rangle - \langle A_R^2 \rangle \end{vmatrix} \tag{2}$$

where A_L and A_R are the voltages measured in the left- and right-circular polarized channels, δ is their relative phase, and $< >$ denotes a time average. Any orthogonal polarization set, such as the H (horizontal) and V (vertical) linear pairing, may also be used to form the Stokes vector terms (Raney 2007). The degree of linear polarization within an elliptically polarized echo (the mixture of unequal circular components) is:

$$\mathrm{DLP} = \frac{\sqrt{S_2^2 + S_3^2}}{S_1} \tag{3}$$

where the total power in S_1 is typically corrected for any system noise component (which is cancelled out by the cross-correlation that yields S_2 and S_3). A strong component of linear-polarized echo indicates scattering from subsurface rocks or rough interfaces beneath smooth mantling material (Stacy 1993; Carter et al. 2004, 2011). The circular polarization ratio, μ_c or CPR, is the ratio between power reflected in the same sense of circular polarization (SC) as that transmitted and the echo in the opposite sense (OC) of circular polarization:

$$\mu_c = \mathrm{CPR} = \frac{S_1 - S_4}{S_1 + S_4}. \tag{4}$$

Given a particular transmit-signal Stokes vector, the full received echo and that for a specific receive polarization can be defined from a 4×4, real-element "Stokes matrix," which captures the relative amplitudes and phases of the surface scattering process. Populating the scattering matrix for each pixel in an image can be challenging—it is accomplished in airborne polarimetric SAR by alternately transmitting horizontal- and vertical-polarization signals, and receiving the complex-valued echoes in the HH, VV, VH, and HV states (hence the term "quad-pol"; van Zyl et al. 1987).

Faraday rotation in the Earth's ionosphere will cause a linear-polarized signal to rotate its angle of polarization on both legs of the trip to the target and back. Early lunar radar observations, by calibrating the linear signal components for this effect, made some of the first applications of the methodology behind using a well-populated Stokes matrix for "imaging polarimetry" (Hagfors & Evans 1968). In this work, the ratio of orthogonal-polarized echo powers was used to estimate the dielectric constant, and thus the approximate density, of the lunar regolith—a result confirmed by in situ studies and lab analysis of returned samples (Carrier et al. 1991). Most subsequent planetary observations transmit a circularly polarized signal and receive both circular

polarization senses of the reflected signal (OC and SC). These more limited observations are typically presented as a Stokes vector (Equation (2)), rather than as a subset of the 4×4 scattering matrix.

From the OC and SC echo power and CPR, a number of geologic inferences can be made, particularly when these measurements are referenced to experience in well-characterized terrestrial settings (Section 4). The OC echoes include strong reflections from smooth, radar-facing parts of the surface, and thus appear most similar to photographs collected under oblique lighting. The SC echoes have little of this "quasi-specular" component, and are dominated by scattering from features that randomize the polarization state, such as rocks or cracks (these echoes are generally split evenly between the SC and OC returns). Using the complete Stokes vector information (i.e., the phase between the SC and OC echoes) can reveal correlations related to the nature of surface scattering (Campbell et al. 1992), the degree of signal penetration (Stacy 1993; Carter et al. 2004, 2006, 2011; Raney et al. 2011), and the terrain slopes along the azimuth direction (Stacy & Campbell 1993).

4. Surface Roughness and Radar Scattering

Radar signals are scattered back to the sensor by surface or subsurface interfaces between materials of different electrical properties, objects such as rocks, or other dielectric discontinuities (e.g., cracks or voids). In general, these variations in the dielectric properties must be physically larger than about 1/10 the radar wavelength to contribute to the scattered signal. As imaging resolution improved, and in particular with the acquisition of Venus data by *Magellan*, a crucial question arose of how to properly describe the mathematical properties of small-scale topography (surface roughness) and how these parameters might relate to the radar observations. If we express surface topography profiles as vertical offset with horizontal position, $z(x)$, we can compute statistical parameters such as the rms height and rms slope, but for almost any natural surface these values will change with the horizontal length scale, Δx, over which they are derived. Since the radar signal is most affected by roughness on scales of about one-tenth the wavelength and larger, the choice of our "ruler" is clearly important to how we model and interpret the echoes. Scale dependent roughness had long been understood in a general sense, but detailed topographic measurements of terrestrial settings that might be good planetary analogs offered the potential to develop a "real world" set of analysis and descriptive techniques (Campbell et al. 1989; Plaut 1991; Gaddis 1992). These studies benefited from the advent of mathematical descriptions of self-affine or fractal behaviors across a wide range of natural processes.

Shepard et al. (1995) noted that self-affine rough interfaces would manifest the types of wavelength-dependent radar

echoes observed in earlier studies, and suggested that a power-law format for the variation in rms height or rms slope could be a powerful means to capture the statistical variability of a surface. The core of this approach is the Hurst exponent, H, which relates the rms slope or rms height to horizontal scale changes with respect to some reference value (often defined at $\Delta x = 1$ m). For example, the rms slope at the scale of the radar wavelength, λ, relative to the rms slope for a sampling interval of 1 m, s_1, is:

$$s(\lambda) = s_1 \lambda^{H-1}. \tag{5}$$

Campbell & Shepard (1996) found that such scaling accurately described the roughness of basaltic lava flows, and that their radar echo strength over a range of wavelength followed the changes in roughness expressed by $s(\lambda)$. The broad applicability of self-affine descriptors to geologic surfaces was documented by Shepard et al. (2001), who used a database of topographic profiles collected by a number of teams in support of *Magellan* data interpretation.

Campbell (2009) developed a general set of empirical correlations between the rms slope at the wavelength scale, $s(\lambda)$, and polarimetric radar echo behaviors for basalt flows on Earth. The HH- or VV-polarized echoes are similar for all but very smooth terrain:

$$\sigma^o_{HH,VV} = 0.16[1 - \exp\{-70.372\, s(\lambda)^2 \exp(-0.0644\phi)\}]. \tag{6}$$

The cross-polarized linear echo is represented by:

$$\frac{\sigma^0_{HV}}{\sigma^0_{VV}} = \frac{1}{3}\left(\frac{\phi}{90}\right)(1 - \exp[-4.5s(\lambda)]) \tag{7}$$

where ϕ is in degrees, and has an asymptotic limit of $1/3$ for very rough surfaces at high incidence angle (Campbell et al. 1993). The ratio of linear and circular "depolarized" components is represented by:

$$\frac{\sigma^0_{HV}}{\sigma^0_{LL}} = 0.3 + 0.2(1 - \exp[-4.5s(\lambda)]) \tag{8}$$

and has an asymptotic limit of 0.5 for rough terrain. The ratio between circular and linear "polarized" components has little dependence on roughness or incidence angle:

$$\frac{\sigma^0_{LR}}{\sigma^0_{VV}} = 0.9. \tag{9}$$

From these relationships we can derive the CPR as a function of roughness and incidence angle (Figure 5).

Many planetary surfaces are characterized by a collection of rocks of varying diameter, on the surface and perhaps suspended within a fine-grained dust layer. Due to the mechanics of rock breakdown, there is commonly a power-law dependence of the number of rocks per unit area on the rock diameter. Power-law values of around -3 are often

observed, in which case 1 m boulders are 1000-fold less numerous on the surface than 10 cm rocks. Radar echoes from such distributions of rocks have been modeled with classical optics approaches (i.e., Mie scattering), and through empirical comparisons with radar echoes measured at a range of wavelengths. In general, the diffuse component of echoes (dominating the SC return) from well-separated surface rocks follows a similar trend to that expected of a "continuous" rough surface with the same rms height (Campbell 2001). Modeling of lunar OC returns has long suggested that much of the radar echo at 70 cm wavelength arises from rocks buried within the dusty regolith (Thompson et al. 1970; Campbell et al. 1997).

In some situations, however, the interfaces or objects on or beneath the surface may not be well described by a continuous form of statistical dependence on horizontal length scale, and the resulting scattering behaviors can appear anomalous. Most relevant to recent studies of the Moon and Mars are cases where dense fields of boulders, either on the surface or buried within a few meters beneath it, behave as double-bounce or corner reflectors. Such features can lead to enhanced back-scatter and very high (up to ∼3) CPR values (Campbell 2012) —clearly well out of the range predicted from Figure 5. Analogs for this type of scattering behavior include blocky silicic lava flows on Earth, such as SP flow in Arizona, which has CPR values of 1–2 depending upon the radar wavelength (Campbell et al. 1993; Campbell 2002). Interpretive ambiguities with such rugged surfaces arise in searches for slab-like ice deposits on planetary surfaces, which can exhibit a coherent backscatter behavior that also produces CPR values up to 2 (Black et al. 2001).

5. Radar Scattering from a Planetary Regolith

The surface of airless bodies is typically covered by a regolith formed of debris produced by the impact of small meteorites. This layer builds up quickly on fresh surfaces (Ghent et al. 2014), and the remaining bedrock is expected to have a very irregular pattern of small- to larger-diameter craters overlain by a mixture of rubble and dust (Shoemaker 1971). Over time, the regolith thickens, the larger-diameter boulders are broken down into fragmental debris and more dust, and the rate of growth slows as only the larger cratering events can reach the bedrock to create new fields of boulders. In the lunar highlands, the regolith is perhaps a few tens of meters deep. In the lunar mare plains, the regolith thickness is highly dependent upon the age of the surface, and may vary from 3–5 m in the youngest (∼2 b.y.) flows to 15–30 m in the oldest terrain (e.g., Wilcox et al. 2005). On Mars, redistribution of fine material by the wind plays a major role in the development of a regolith cover, and on Venus impact fines can reach up to 2000 km downrange of the crater due to high-altitude wind transport.

Radar backscatter from a regolith predominantly arises from rocks on the surface, "volume" echoes from rocks suspended
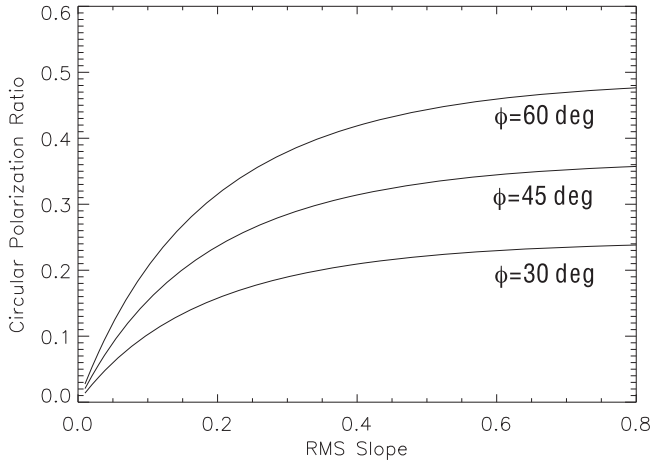
Figure 5. The circular polarization ratio (CPR) for basaltic lava flows as a function of wavelength-scale rms slope predicted by Equations (6)–(9). The three lines represent behaviors at three values of the radar incidence angle, ϕ.
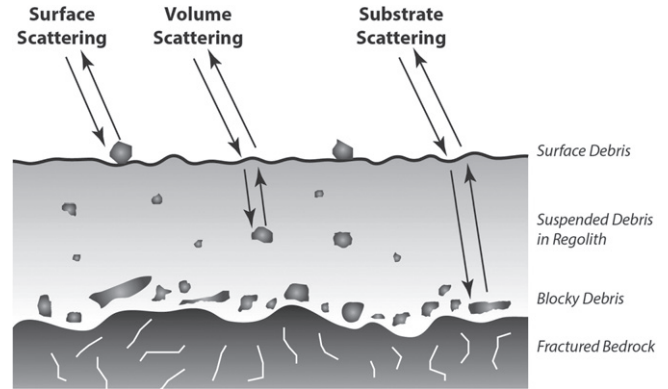

Figure 6. Schematic of radar scattering from a planetary regolith (Campbell et al. 2014). The relative importance of surface, volume, and substrate scattering will vary with the regolith thickness, composition, and the illuminating radar wavelength.

within the fine-grained debris, and reflections from the interface between the soil and the disrupted bedrock substrate (Figure 6). The total radar echo, expressed as a dimensionless backscatter coefficient, σ^0, is (Campbell et al. 2014):

$$\sigma^0 = \sigma^0_{\text{surface}} + \sigma^0_{\text{volume}} + \sigma^0_{\text{substrate}}. \tag{10}$$

The relative importance of each component to the overall echo varies considerably with radar wavelength due to changes in the relevant rock populations and attenuation losses in the regolith. Both the volume and basal-interface components are modulated by the microwave loss tangent, the ratio of the imaginary component of the complex dielectric permittivity to the real component ($\tan\delta = \varepsilon''/\varepsilon'$), of the soil. Variations in the real part of the dielectric constant are primarily driven by the density of the material, with poorly consolidated sediments having values of 2–3 and solid rock reaching $\varepsilon' = 8$–12. Variations in the imaginary part, and thus the loss tangent, are modulated by the composition of the material and the environmental conditions. On Earth, liquid water mixed with salts can create highly lossy conditions. For the Moon and Mars, the lack of such water means that losses are driven more by the abundance of particular iron and/or titanium-bearing minerals. On Venus, the 450 K environment plays a major role, since loss properties increase with temperature for geologic materials. Water ice well below the freezing point has very low microwave losses, allowing an incident signal to have the long path lengths required to produce a strong coherent backscatter effect from internal voids or other scattering features (Black et al. 2001).

We can examine the impact of loss variations with a simple model of a soil layer of thickness h, with uniform rock population as a function of depth, overlying a rough interface that represents the transition to fractured, in-place bedrock

(Figure 6). Echoes from the basal region are attenuated by passage through the soil (Campbell 2002):

$$\sigma^0_{\text{substrate}} = \sigma^0_{\text{vacuum}} T^2 R \exp\left[-4\alpha h/\cos\theta\right] \tag{11}$$

where σ^0_{vacuum} is the backscatter coefficient of an interface of equivalent roughness exposed at the surface, T is the Fresnel transmission coefficient of the regolith/vacuum interface, R is a loss term related to the diminished reflectivity contrast between soil and rock versus rock and vacuum, and θ is the angle between the transmitted ray and the surface normal. The loss factor, α, for small values of the loss tangent, is:

$$\alpha = \frac{2\pi}{\lambda}\left[\frac{\varepsilon'}{2}(\sqrt{1+\tan\delta^2} - 1)\right]^{1/2} \approx \frac{\pi\sqrt{\varepsilon'}}{\lambda}\tan\delta. \tag{12}$$

The real dielectric constant of the upper lunar regolith is about 2.7 (Carrier et al. 1991), so T^2 is ~0.86. Taking approximate values of $\varepsilon' = 8$ for the rocky material and $\varepsilon' = 3$ for packed soil, R is ~0.25. For volume scattering by rocks suspended in the soil, the effect of the losses is averaged over the probing depth of the radar (Campbell 2002):

$$\sigma^0_{\text{volume}} = \sigma^0_{\text{rocks}}\frac{T^2\cos\theta}{4\alpha}\left[1 - \exp\left(\frac{-4\alpha h}{\cos\theta}\right)\right] \tag{13}$$

where σ^0_{rocks} is the total backscatter coefficient of rocks of all relevant sizes (diameters larger than about one-tenth the radar wavelength) within a unit volume.

Based on these expressions, we can understand the variability in radar echoes from a planetary regolith as a function of wavelength. Short wavelengths (X-band or 3–4 cm) penetrate less than a meter, and are scattered by even quite small (sub-cm diameter) rocks. Since these rocks are typically far more numerous in ejecta than rocks of decimeter to meter diameter (Section 4), X-band images often show a strong signature from the abundant small impact crater population on any airless
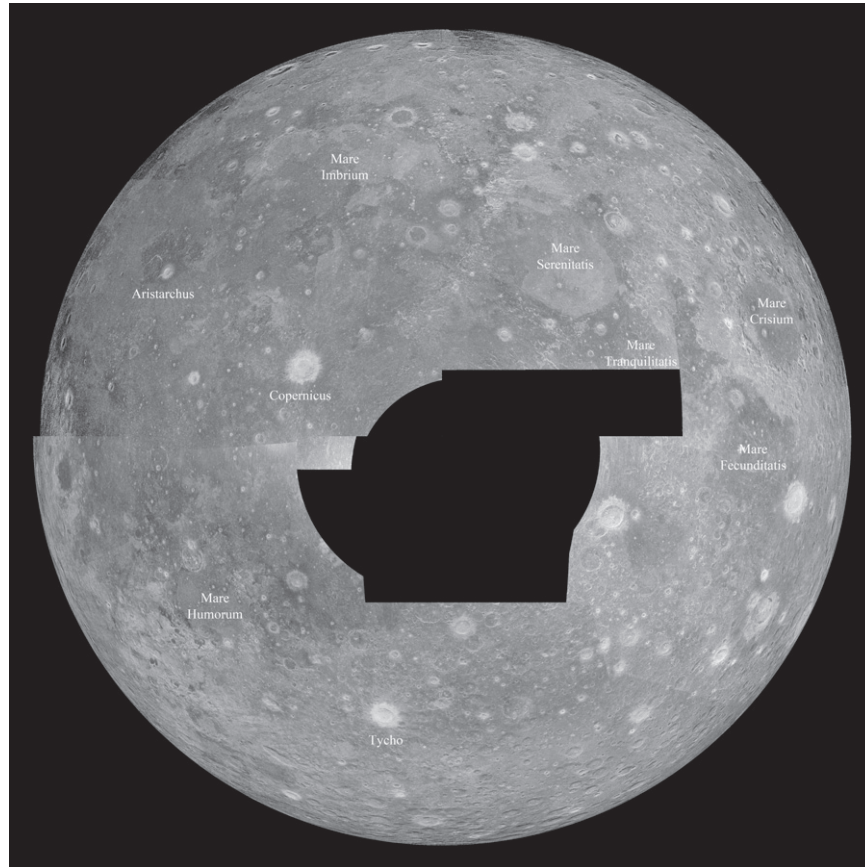
Figure 7. Mosaic of 70 cm radar image coverage using 3 μs pulse length and same-sense circular polarization. Orthographic view of the lunar near side; these data are available through the NASA Planetary Data System.

surface. At long wavelengths (P-band or $\sim$70 cm), the penetration depth is several meters or more, and the relevant population of rocks is much smaller, so we often see a strong influence of regolith composition and (under favorable conditions) the nature of the substrate. Between these end-members, C-band or S-band observations can mix these behaviors depending on the soil chemistry and proximity to craters.

6. Focused Radar Observations: 2001–2015

Preliminary work by Stacy (1993) and Stacy et al. (1997) showed that focused, SAR-like processing could yield significant improvements in the resolution of Earth-based lunar radar maps. Immediate application of these techniques was hampered, however, by the Arecibo setup after the late 1990s, which did not allow measurement of both senses of circular-polarized echoes for 70 cm signals, and by the inability of the 12.6 cm system to rapidly shift from transmit to receive for lunar round-trip times. We initiated high-resolution proof-of-concept observations, with the Arecibo 70 cm system operating in a single polarization mode, in 2000 November. With the commissioning of the Green Bank Telescope, it became possible to receive dual-polarization signals from the Moon for both wavelengths, leading to a series of mapping projects.

At 70 cm wavelength, the primary goal was to obtain relatively complete coverage of the near side of the Moon at a spatial resolution about a factor of ten finer than that of the last dual-polarization Arecibo mapping in 1986 (Thompson 1987). The observations were carried out from 2003 to 2007 using an uncoded, 3 μs pulse and a 17 minute coherence interval for each of the 3–9 independent looks collected for each region. The use of the uncoded signal was advantageous in allowing a clear period of noise measurement during each interpulse period, and in avoiding a range-compression step in the processing. Focused processing was successful based on the ephemerides, and a total of about twenty separate "beam patterns" on the near side yielded a well-calibrated, dual-polarization map at 400–600 m spatial resolution (Figure 7; Campbell et al. 2007).

In 2009, we began to collect 70 cm data with 1 μs time resolution, using a 13-element, Barker-coded signal (Evans 1968). By using a coherence interval of about 40 minutes, we obtain single-look images with spatial resolution of about
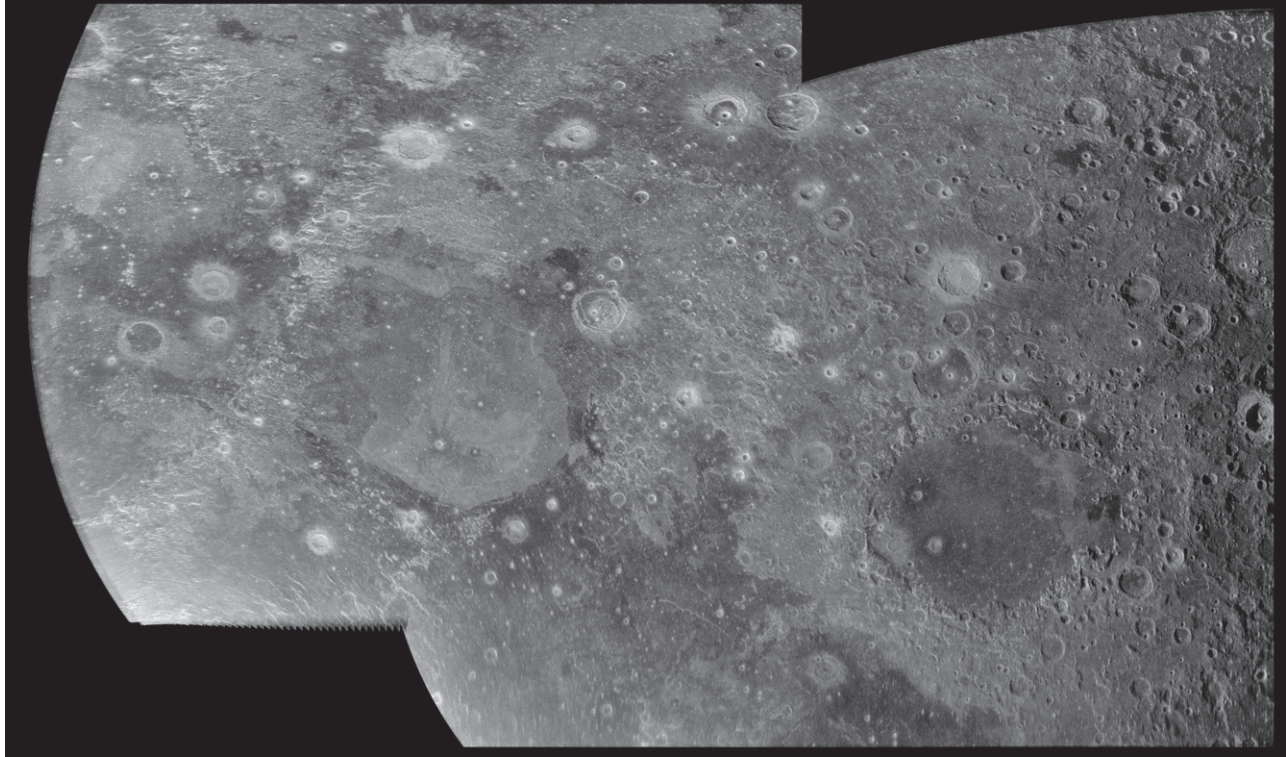
Figure 8. Coverage at 200 m spatial resolution for the northern lunar maria with the Arecibo 70 cm wavelength radar system. Same sense circular polarization. Most of Mare Imbrium is covered at upper left, and Mare Crisium is at lower right. Parts of Mare Tranquilitatis are visible at lower center.

200 m pixel^{-1}. Despite the shorter baud, the increase of about a factor of four in pulse length (from 3 to 13 μs) offsets the lower echo strength of the smaller surface resolution cells. Observations on multiple days are added to obtain a 5- to 9-look final product to reduce speckle effects (Campbell et al. 2014). To date, we have obtained coverage of many of the nearside mare regions (Figure 8) and the north pole with this higher spatial resolution.

For the 12.6 cm (S-band) wavelength, the transmitter is capable of a time resolution as fine as 0.1 μs, corresponding to ~20 m horizontal resolution cells on the surface when matched to a coherence interval of about one hour. The transmitted signal was modulated with a PN code of length 131071 (filling the interpulse period, as opposed to the short duty cycle of the 70 cm transmissions). Doppler sharpening to the desired accuracy was not readily achieved from the ephemeris predictions alone, so we added an autofocusing step to the processing that compensates residual phase errors (Figure 3) (e.g., Wahl et al. 1984). Only a small number of maps in this format were collected, due in part to the significant processing burden and the limitation of sampling at 1 bit in the A/D system available at the GBT during this period. Our subsequent work moved to a 0.2 μs baud and a 65535-length PN code, for which 4 bit sampling could be employed. With a 29 minute

coherence interval, we could average in azimuth and range to obtain a 4-look, 80 m resolution final product (Campbell et al. 2010). Coverage to date in this mode is available through the PDS for the nearside and polar regions (Figure 9).

In general, for the 4 bit 12.6 cm and 70 cm observations we achieve a robust calibration of the SC and OC data to their respective system and thermal noise backgrounds, and thus deliver a reliable estimate of the CPR. We did find that the transmitted signal level must be limited to about 60 kW for the S-band observations to keep the signal and the noise within the dynamic range of 4 bit A/D encoding. Absolute calibration of the data to the dimensionless backscatter coefficient appeared to work well for the 3 μs pulse, 70 cm wavelength data (Campbell et al. 2007), but estimates for the S-band signals (Campbell et al. 2010), while consistent among the coverage areas (Figure 9), remain significantly different from earlier disk-integrated values (Hagfors 1970).

7. Science Applications

7.1. Permanently Shadowed Polar Terrain

The Moon's spin axis is inclined at a small angle to the ecliptic plane, so topographic depressions near the poles can be in permanent shadow from solar illumination. Earth-based
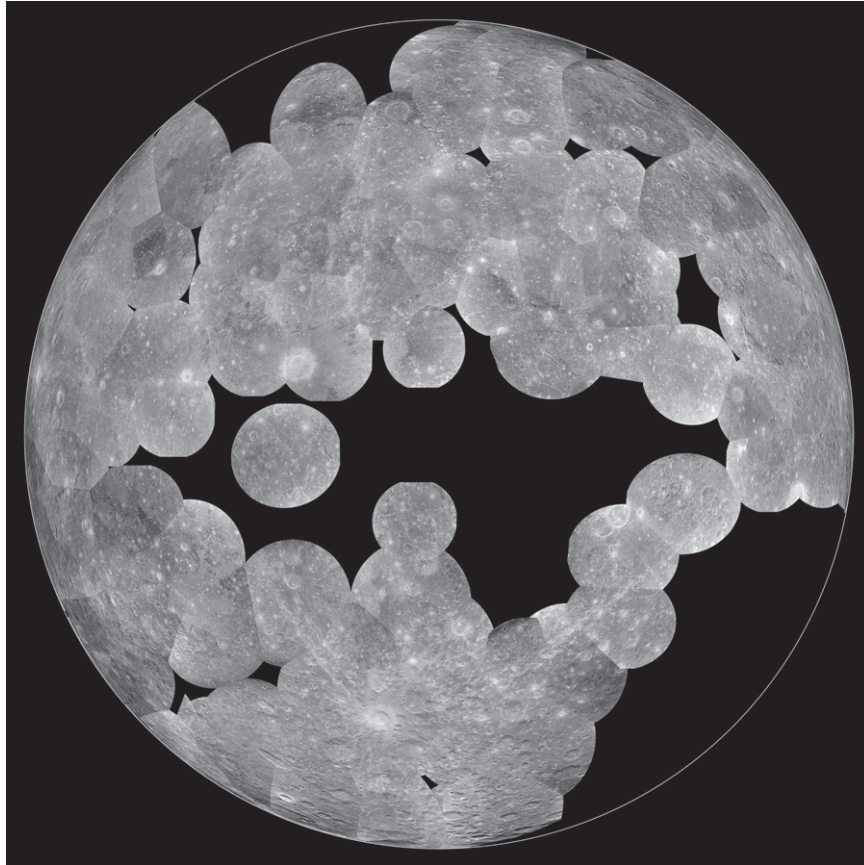
Figure 9. Coverage of the Moon's near side with the 12.6 cm Arecibo radar system through 2015. Same sense circular polarization, 80 m horizontal spatial resolution.

radar measurements (e.g., Slade et al. 1992; Harmon et al. 2011) reveal high-CPR scattering properties from similarly shadowed areas at the poles of Mercury that appear to be consistent with water ice, presumably delivered by cometary impacts. Renewed orbital investigations of the Moon, beginning with the Lunar Prospector mission, have sought to identify any similar water ice trapped at the poles (Feldman et al. 2001; Nozette et al. 2001; Spudis et al. 2010). Prior to the acquisition of orbital laser altimetry, Earth-based interferometric radar observations provided the best guide to the locations of these shadowed areas (Margot et al. 1999, 2000). Earth-based imaging radar also plays an important role because the lunar libration allows observations with a view up to about $7°5$ above the horizon at the poles. In both Earth-based and orbital radar investigations, the CPR is of great interest, since values of 1–2 are expected for scattering in slab-like ice, though again potentially ambiguous with rugged, boulder-strewn surfaces.

Observations at 12.6 cm wavelength by Stacy et al. (1997) showed that the Moon's south pole offered no evidence for contiguous regions of high CPR that were obviously coincident with the outline of permanently shadowed terrain—the hallmark of ice on Mercury. For example, crater interior walls

sometimes exhibit high CPR, but this behavior persists from the shadowed bottom to the seasonally sunlit upper scarps. In the larger areas of permanent shadow on the floors of craters like Shoemaker or Amundsen, high-CPR features are correlated with small (few-hundred meter diameter), fresh crater ejecta. Both observations seem more consistent with radar scattering by rocky debris rather than slab-like ice. These conclusions were confirmed in greater detail by 20 m resolution 12.6 cm mapping (Figure 10; Campbell et al. 2006).

Mapping with the 70 cm system showed that no high-backscatter, contiguous signatures emerged with the greater penetration depth of the longer radar wavelength (Campbell et al. 2003). The correlation of localized high-CPR signatures with small craters was again distinct, and patches of such behavior occur in both sunlit and shadowed terrain mapped by earlier investigators as related to impact melt sheets (Figure 11). The interpretation is that Orientale Basin ejecta, with a substantial component of melt, was deposited across the south polar region and flowed into topographic lows. The existence of this material at the base of the regolith, rather than a much thicker, ancient dust layer, allows small craters to excavate rocky debris that produces the higher CPR values (Campbell &
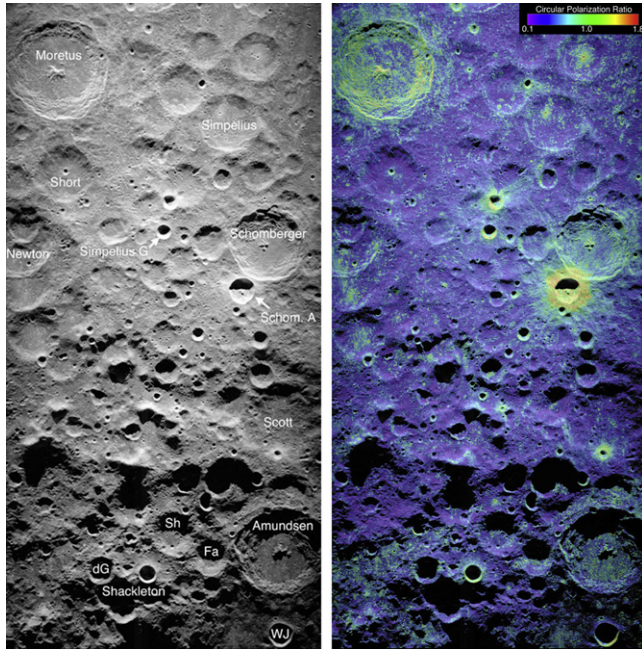
Figure 10. Radar image of the southern highlands and polar region of the Moon at 12.6 cm wavelength (left). The pole is located near the rim of Shackleton crater. On the right is an overlay of the image with values of the circular polarization ratio, showing the high values linked with fresh crater ejecta. The floors of craters like Shoemaker (Sh), Faustini (Fa), and Amundsen do not exhibit high-CPR signatures strongly correlated with the margins of the permanently shadowed terrain. Adapted from Campbell et al. (2006).
(A color version of this figure is available in the online journal.)

Campbell 2006). To date, there is thus no clear evidence for slab-like (meter-scale thickness, >100's of meters in horizontal extent) ice in lunar polar craters visible to Earth-based radar. This finding is consistent with evidence from neutron spectrometer hydrogen mapping and the LCROSS impactor study, which suggest that water ice is present at levels of perhaps a few weight percent in the upper meter of the regolith.

7.2. The Maria

Most large impact basins on the nearside of the Moon are filled by basaltic lava flows that erupted over hundreds of millions of years, forming the distinct dark patterns of the lunar maria. Flows differed substantially across the Moon in their chemistry depending upon their sources within the crust, and over time from any one source as the magma chambers fractionated and cooled. Understanding subtle changes in composition among the flows is a key aspect of tracing the thermal history of the mare-forming period, and particularly in identifying discrete units for estimation of relative ages (e.g., Hiesinger et al. 2000). Imaging radar has long contributed to these studies, and recent high-resolution maps show that 70 cm

data can reveal even subtle changes in lava composition (Figure 12).

Schaber et al. (1975) noted that 70 cm wavelength, SC-polarization radar echoes were significantly lower in some of the youngest flows within Mare Imbrium, and attributed this effect to enrichment of the mineral ilmenite ($FeTiO_3$). Correlation of later maps with estimates of the titanium content from multi-spectral data showed a consistent inverse correlation with 70 cm SC echo strength across the near side (Campbell et al. 1997), but this simple correlation did not hold for some parts of Maria Imbrium and Serenitatis (Campbell et al. 2009b). More detailed analysis shows that the 70 cm echoes exhibit strong swings in brightness with minor changes in flow TiO_2 content when the fractional abundance of ilmenite is low (<4%–5%). The reason for this exaggerated response is that when the ilmenite content is low, the radar echo has a significant component from the substrate region at the base of the regolith (Figure 6). As a comparison of Equations (11) and (13) shows, substrate echoes are more strongly affected by small changes in the loss tangent of the dust, and thus the radar image variations are more dramatic. Mapping of the changes in radar brightness across the basin clarified boundaries between major flow complexes, suggested the presence of a large, now-buried graben structure in northern Serenitatis, and revealed linear segments of apparently deeper regolith inferred to be collapsed lava tubes (Campbell et al. 2014).

Remote sensing studies of the lunar highlands suggest that basaltic volcanism had already begun during the final period of basin-forming impact bombardment (e.g., Schultz & Spudis 1979). Now hidden by feldspar-rich material of the highlands, these "cryptomare" units represent an additional component of the early volcanic record of the Moon. The deep probing allowed by the 70 cm wavelength radar has added significantly to our understanding of these ancient lava flows. In general, the lunar highlands have higher 70 cm radar echoes than the mare plains, despite a much thicker regolith and fewer near-surface rocks. The low iron and titanium content of the highland soils allows much greater penetration, so even the smaller population of suspended rocks can lead to higher radar returns (Thompson et al. 1970). Campbell & Hawke (2005) found areas east of the Orientale basin where highland material mapped at the surface from multi-spectral methods had much lower 70 cm radar echoes than expected. These areas connected with mare-contaminated highland material mapped by Mustard & Head (1996) near the edge of Oceanus Procellarum, showing that the cryptomare units must extend a long distance beneath the Orientale ejecta (Figure 13). Similar work in other regions has used the long-wavelength radar data to improve mapping of cryptomare unit outlines (Hawke et al. 1993).
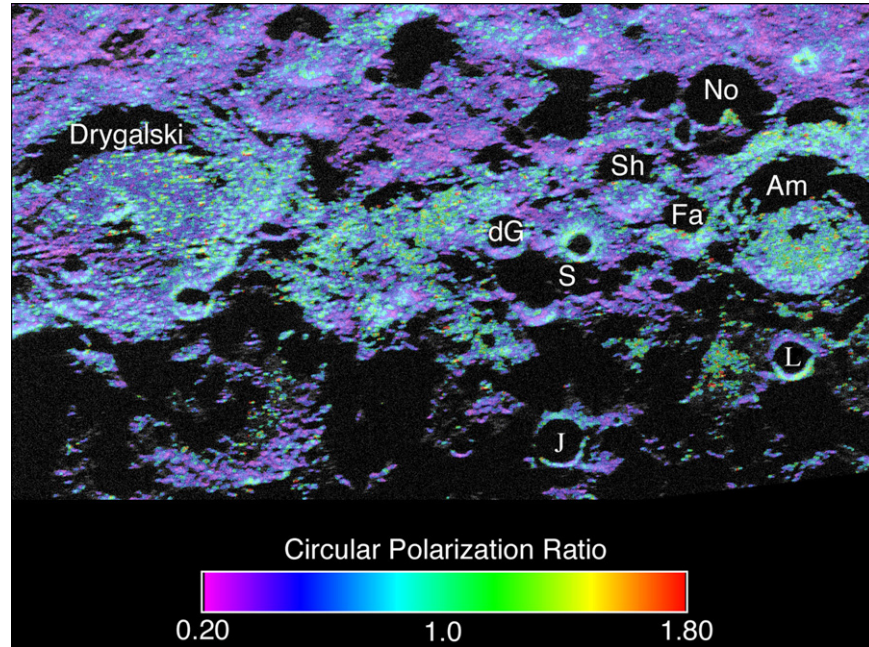
Figure 11. Radar image of the south polar region of the Moon at 70 cm wavelength overlain with color values for the circular polarization ratio. Patches of higher CPR correlate with small fresh craters in sunlit and shadowed areas, and appear to be due to local excavation of impact melt material emplaced during the Orientale Basin impact (Campbell & Campbell 2006).
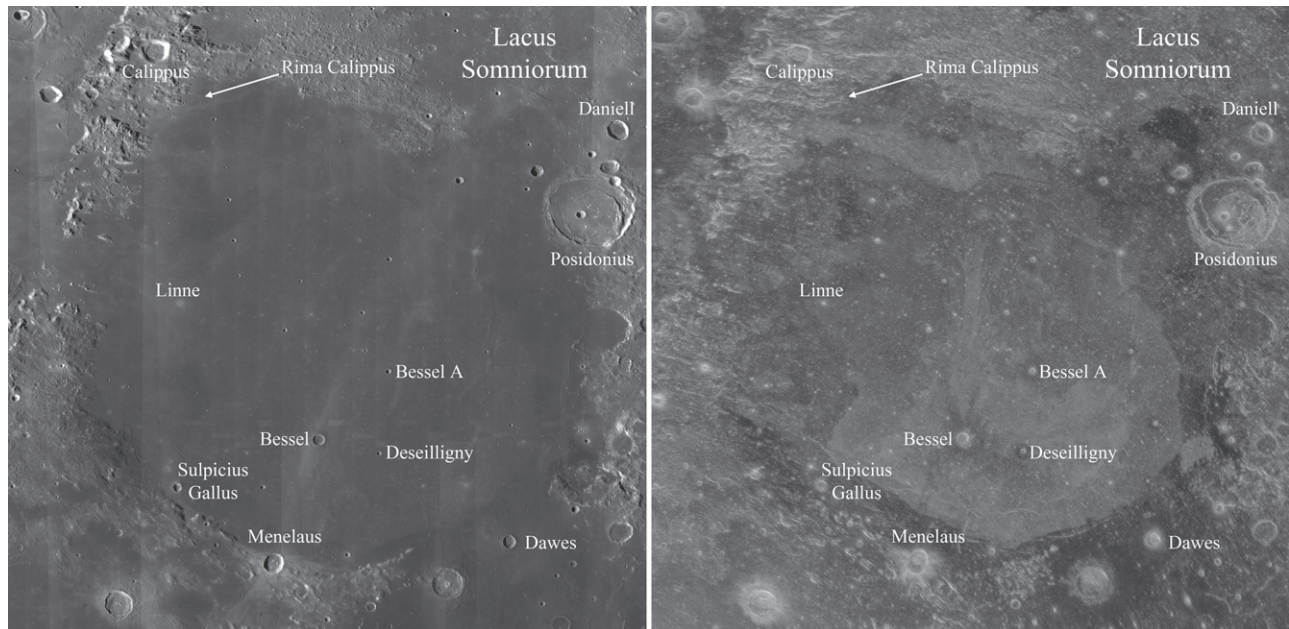(A color version of this figure is available in the online journal.)

Figure 12. Comparison of visible (left) and high-resolution 70 cm radar (right) views of Mare Serenitatis. The long-wavelength, SC polarization radar view detects very subtle changes in the ilmenite content of basalt units, revealing an intricate pattern of flow boundaries not evident in other data sets (Campbell et al. 2014).
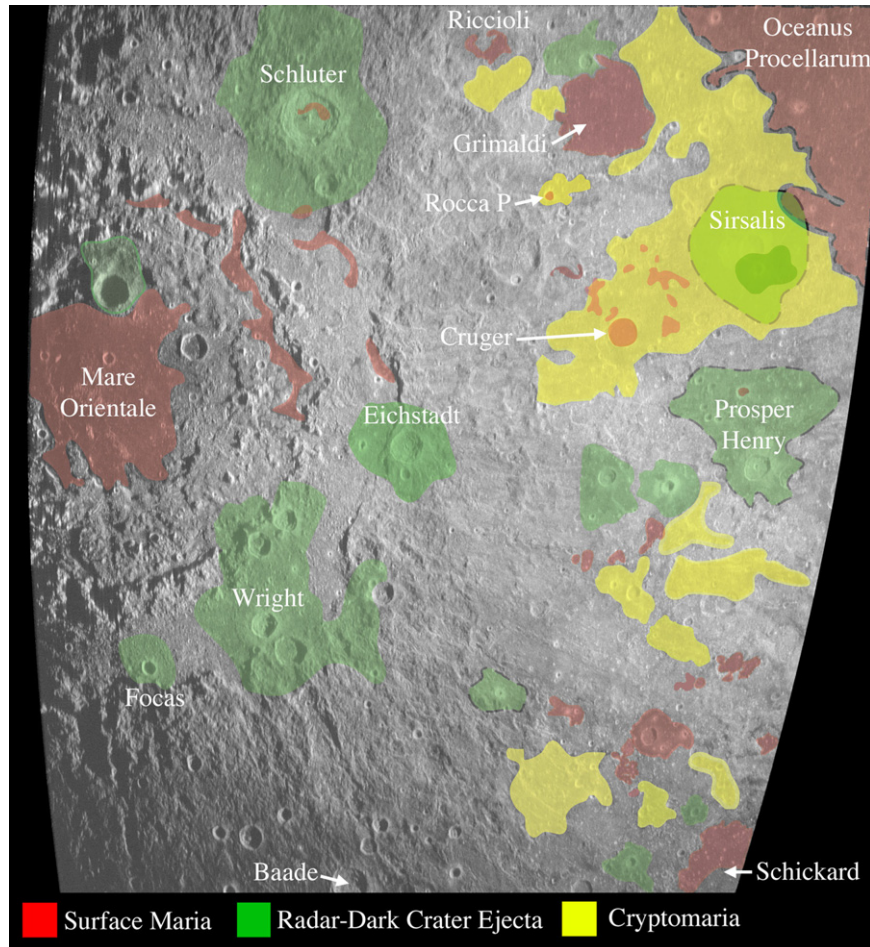
Figure 13. 70 cm radar map of the region east of Orientale basin (0°–45° S, 55°–105° W), color-coded to show locations of ancient basalt deposits (cryptomaria) buried by feldspar-rich basin ejecta (Campbell & Hawke 2005). Red tones show mare basalts exposed at the surface, and green outlines note fine-grained ejecta of younger impact craters.
(A color version of this figure is available in the online journal.)

7.3. Volcanic Complexes

Within the broad plains of the maria are isolated volcanic features that exhibit much more diverse formation mechanisms. These include the Mons Rumker Formation, the Marius Hills dome fields, and a host of other dome-like or pitted structures. The numerous domes of the Marius Hills, long noted as being quite different from typical mare plains-forming eruptive features, exhibit surprisingly high CPR values (Figure 14) that indicate a blocky flow structure preserved beneath the regolith cover (Campbell et al. 2009a).

The Aristarchus Plateau has been of enduring interest for Earth-based radar studies (Zisk et al. 1977; Gaddis et al. 1985; Campbell et al. 2008). Early mare-forming eruptions released large amounts of volatiles (like CO or CO_2) from the magma chambers to create explosive, fire-fountaining events in the

lunar vacuum. The magma in these fountains was widely dispersed as fine-grained, glassy particles to form "localized" or "regional" pyroclastic deposits. The material erupted on the Aristarchus Plateau, a 200×200 km topographic high in Oceanus Procellarum (Figure 14), is the largest preserved regional deposit.

Radar image data are particularly suited to mapping fine-grained, rock-poor material, like the pyroclastics, on "rougher" background terrain. The pyroclastic deposits have only those rocks excavated by craters that penetrate to the underlying pre-existing regolith and bedrock, and their surface roughness is minimal. As such, they appear radar-dark even at short (3.0–3.8 cm) wavelength, and especially so in the SC echo mode (Zisk et al. 1977, 1991; Gaddis et al. 1985; Hawke et al. 1990; Carter et al. 2009). For the Aristarchus Plateau, this overall impression of a draped, fine-grained deposit was greatly
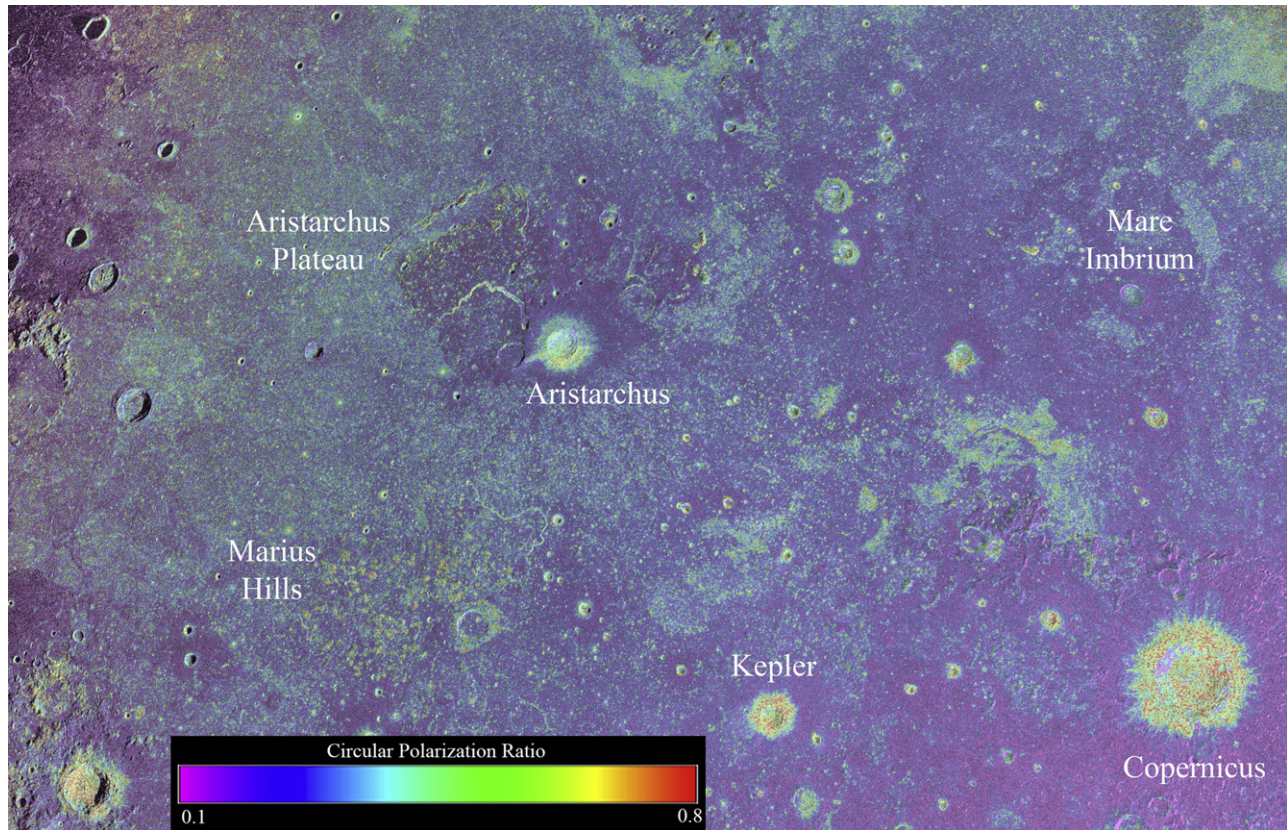
Figure 14. 70 cm wavelength, OC-polarized radar image of north-central Oceanus Procellarum, overlain with color tones of the circular polarization ratio (CPR). Note the high values (red and orange tones) associated with the Marius Hills dome field and the ejecta blankets of younger craters such as Copernicus, Kepler, and Aristarchus.

(A color version of this figure is available in the online journal.)

augmented by the collection of high-resolution radar data at 12.6 and 70 cm wavelengths.

In the new maps, the overall low-SC signature noted in earlier studies (Zisk et al. 1977) is shown to have two distinct behaviors. Over much of the plateau, the 70 cm return is very low, punctuated only by rocky debris surrounding small craters that have reached the underlying terrain. In patches that extend from the edges of the large sinuous rille (Vallis Schroterii) that cuts the plateau, the echo is significantly higher (Figure 15). These areas of higher 70 cm radar return were inferred to be the locations of overspill from the rapid flow of magma that filled and partially carved the rille (Campbell et al. 2008). In the high-resolution ($25 \, \mathrm{m \, pixel^{-1}}$) images collected at 12.6 cm wavelength, there are similar enhanced radar echoes peripheral to the rille, but over only a portion of the total area mapped from the 70 cm echoes (Figure 16). The shorter-wavelength enhancements are assumed to arise where the pyroclastic deposit is most shallow, so that even small-diameter craters can excavate and mix rocky debris into the upper few meters. From these new images we have a much more detailed view of the complex eruptive history of the Aristarchus Plateau.

7.4. Impact Ejecta and Melt

Impact cratering is the fundamental mechanism that erodes and modifies landscapes on the Moon and other airless bodies. Craters of some diameter, D, are typically assumed to excavate and redistribute material from a depth of about $D/5$ to $D/10$ below the surface. If this depth of excavation can reach the bedrock beneath the regolith, then the crater ejecta is typically quite rocky, and thus radar-bright, within about $D/2$ radial distance from the center of the cavity (note the very high radar echo and CPR of Copernicus crater in Figure 14). Additional fragmental material is ejected on long ballistic trajectories to make "rays" that may reach to hundreds of kilometers or greater distance (Hawke et al. 2004; Wells et al. 2010). An interesting feature of younger craters is a concentric "halo" of low radar return that appears to comprise material of much lower decimeter-scale rock abundance than the typical background lunar regolith (Figure 17). The implication is that the
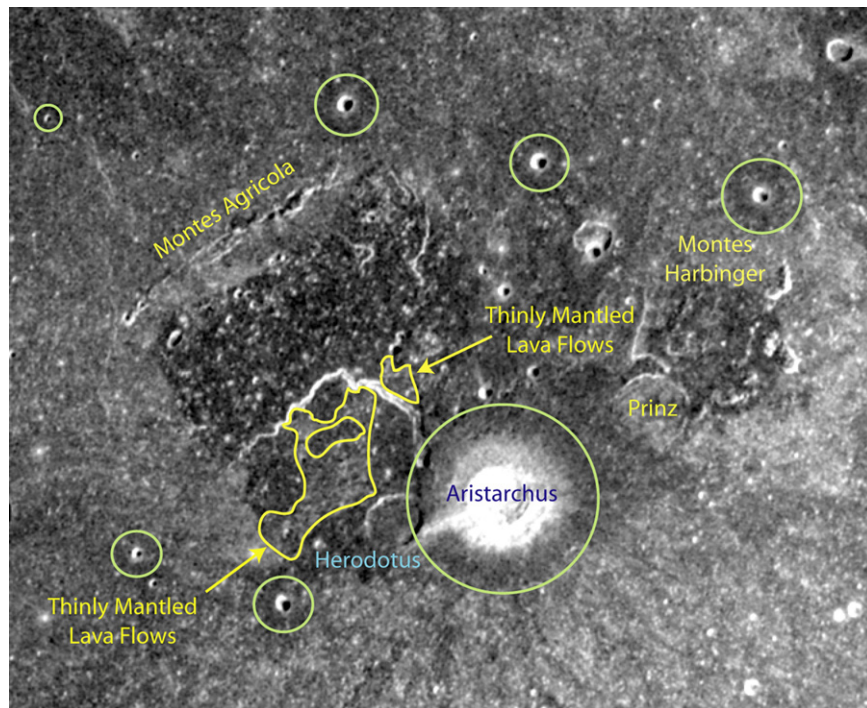
Figure 15. 70 cm wavelength, SC-polarization radar view of the Aristarchus Plateau (Campbell et al. 2008). The dark regions are mantled by up to 30 m of fine-grained pyroclastic material. Areas outlined in yellow peripheral to the bright sinuous rille are perhaps 5–10 m thick, underlain by lava flows erupted during the fire-fountaining period. Green circles are crater-related fine-grained ejecta deposits.
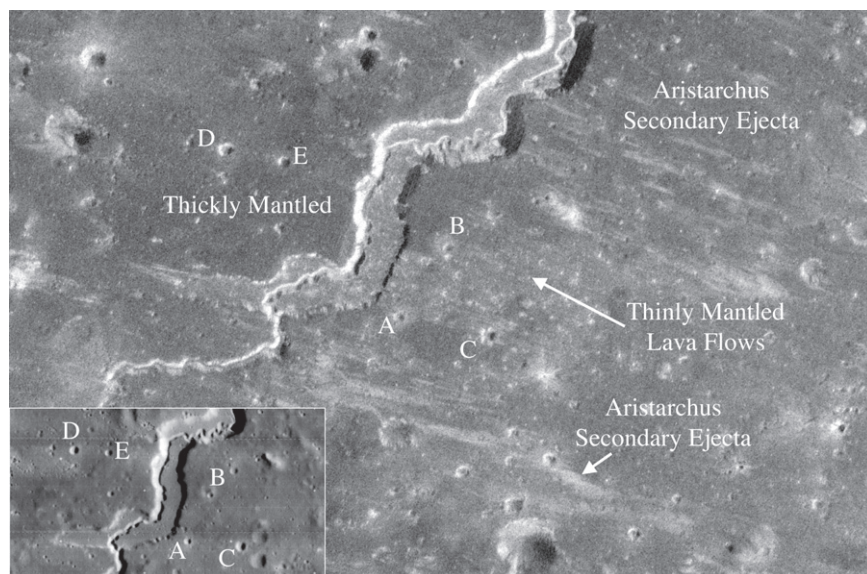(A color version of this figure is available in the online journal.)

Figure 16. 12.6 cm wavelength, SC-polarization radar view of a region near the terminus of Vallis Schroterii on the Aristarchus Plateau (Campbell et al. 2008). Inset view is from Lunar Orbiter IV image, with small craters noted to match the labeling of the radar image.
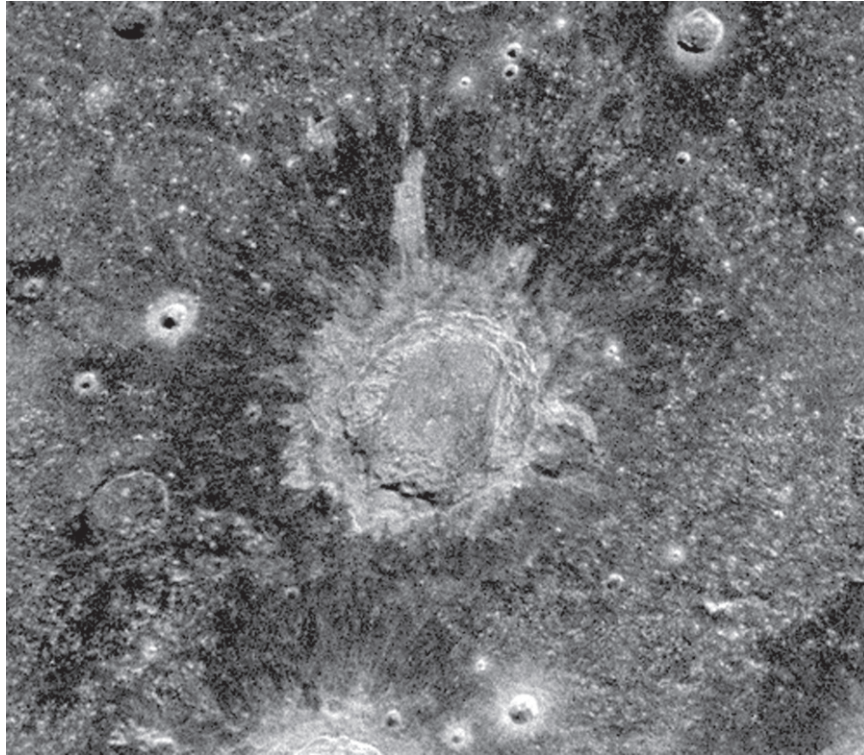
Figure 17. 70 cm wavelength, SC-polarization radar image of low-radar-return ejecta halo surrounding the 87 km diameter lunar crater Aristoteles. Note the azimuthally asymmetric pattern of both the radar-bright and radar-dark ejecta.

cratering process creates a highly comminuted portion of the ejecta that is preferentially deposited within this radial range. Ongoing regolith development mixes the finer-grained component into the background and excavates new rocks from below, so over time the dark haloes disappear (Ghent et al. 2005, 2008; Thompson et al. 2006).

Crater formation also generates a fraction (on the order of a few percent) of ejecta that is melted. Much of this melt remains within the final crater cavity as ponds or flows on the floor and walls. As the crater diameter increases, more melt can exit the crater, often in a highly asymmetric radial pattern due to the rim topography and arrival geometry (oblique versus vertical impact angles) of the impactor. We discussed above the role of basin-scale impacts in creating impact-melt sheets in the south polar region of the Moon, and how radar images at different wavelengths can be used to understand the production of small-crater debris from these rocky units. At the scale of individual craters, radar imaging can also greatly enhance the discrimination of melt sheets and flows to better understand the dynamics of crater formation.

Melt deposits on the floors of younger craters like Tycho have platy, rugged surface morphology that resembles rapidly emplaced lava flows. These rough surfaces have very high radar backscatter, noted in the earliest Earth-based imaging studies (Pettengill & Thompson 1968). As imaging resolution improved, similar rugged flows and ponds could be discerned outside of the craters. In some cases the melt is concentrated in a single major flow from a small gap in the rim, often with channel or ridge-like features similar to lava flows (Figure 18). In other cases there are many narrow flows emerging from the proximal ejecta, suggesting that the melt overtopped the rim over a broad area (Figure 19). For the Glushko melt in particular (Figure 18), the CPR values of ~1 (Campbell et al. 2010) are much higher than observed for even rough basaltic lava flows (Figure 5). This suggests a much more dense collection of surface and shallow-buried roughness elements (blocks, plates, or boulders), similar to the properties of blocky lava flows like SP (Section 4).

The major advantage in such radar mapping of impact melt is the ability to penetrate the shallow (few-meter at most) regolith developed above the melt and discern the residual rough morphology of the partially eroded flows (Campbell et al. 2010). In many cases, such detailed flow outlines cannot be mapped from visible images alone, since the regolith mutes and subdues their morphologic signatures. This provides a strong argument for using imaging radar to map similarly buried geologic features on Mars or the asteroids. Particularly in studies using two or more wavelengths (e.g., 3.8 cm,
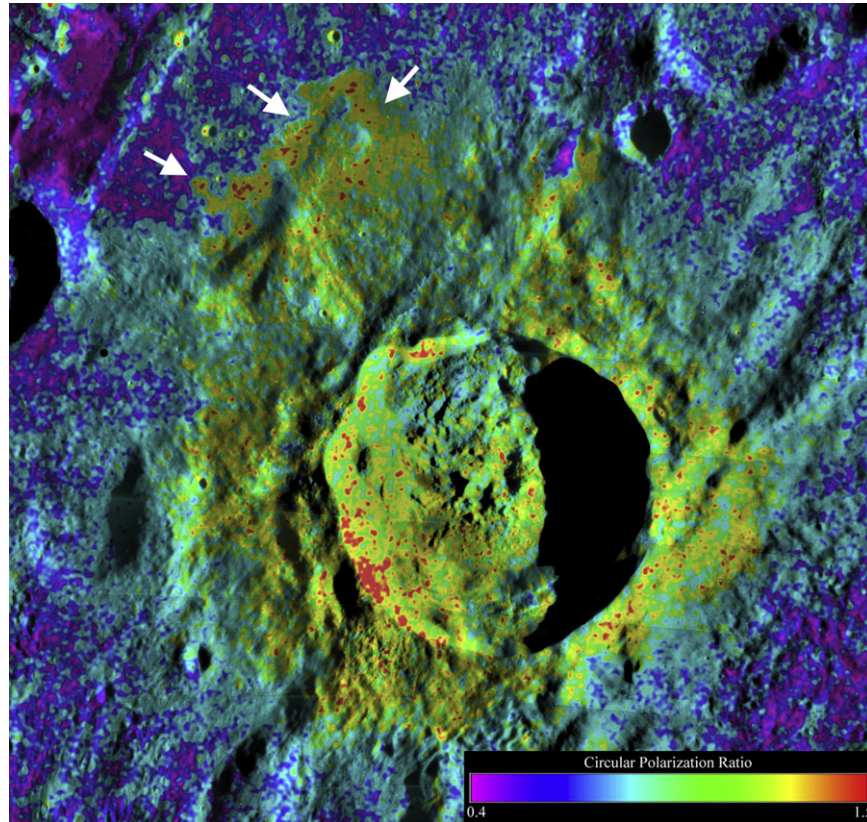
Figure 18. A color overlay of S-band (12.6 cm wavelength) circular polarization ratio on OC image base for the 43 km diameter crater Glushko. Arrows denote a large outflow of impact melt from the crater, which has CPR values typical of blocky or platy terrestrial lava flows (Campbell et al. 2010).
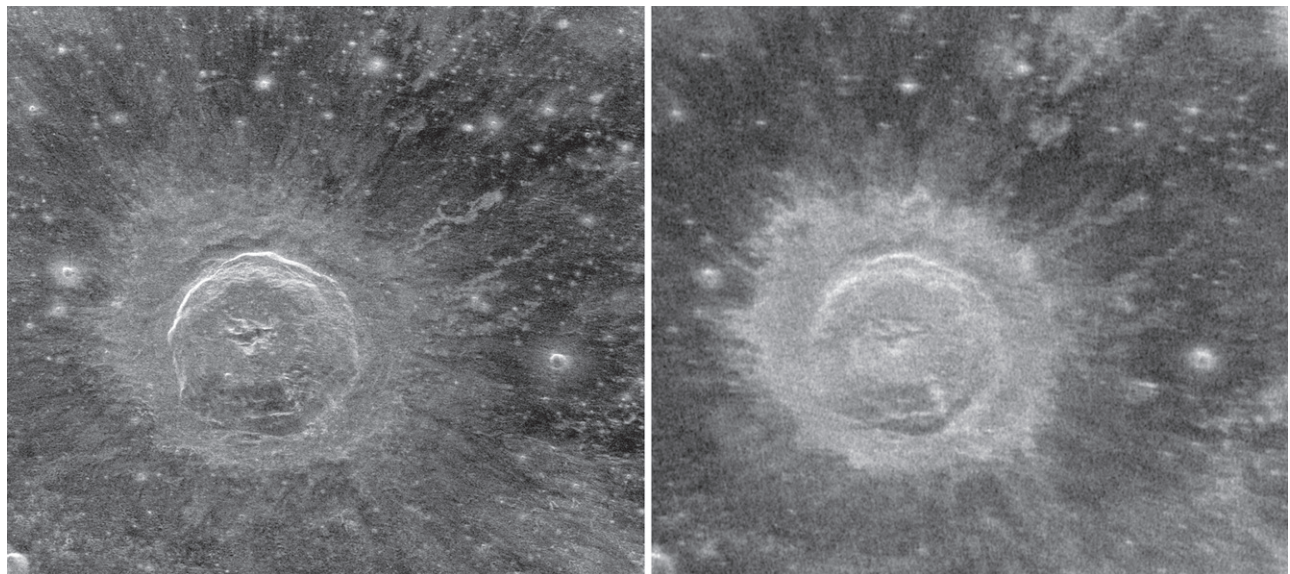(A color version of this figure is available in the online journal.)

Figure 19. Radar images of the 55 km diameter lunar crater Aristillus at 12.6 cm (left) and 70 cm (right) wavelengths, SC polarization. Note the radar-bright impact melt flows northeast of the crater near-rim deposits. The 70 cm echoes from the crater interior and near-rim ejecta are higher due to the penetration of thin regolith cover by the longer radar wavelength.

12.6 cm, and/or 70 cm; Thompson et al. 1979), these examples and that of the polar crater floors show how polarimetric radar image data can enhance our three-dimensional understanding of the impact process, its effect on the original terrain, and of crater and ejecta modification over time.

8. Summary and Future Directions in Planetary Radar

We have reviewed scientific investigations of the past fifteen years that used Earth-based radar imaging of the Moon, built on the broader understanding of radar scattering from natural surfaces derived from terrestrial fieldwork and airborne/ spaceborne radar data since the late 1980s. Some parallels between the lunar work and other studies are noted above, such as the search for ice deposits in permanently shadowed polar craters on Mercury and the Moon. In this section, we discuss additional connections between terrestrial and lunar radar studies and those of the inner planets, small bodies, and outer planet satellites. Finally, we consider new directions in planetary radar imaging, looking toward the next generation of orbital sensors and methods.

There is a strong connection between studies of crater-derived deposits on the Moon, our nearest touchstone to understand this process, and reconstructing the geologic evolution of other bodies across the Solar System. Radar studies of craters on the Moon, and particularly their fine-grained haloes and rugged impact melt flows, provide significant insight into similar deposits on Mars (observed in both radar and thermal infrared measurements) and Venus (Ghent et al. 2010; Harmon et al. 2012). The extensive distribution of melt deposits from large lunar craters (Campbell et al. 2010; Carter et al. 2012) suggests that similar deposits may have been widely present across early Mars, and detection of more localized deposits around craters such as Aristillus and Glushko helps to bridge the gap in scale to the much larger outflows surrounding craters on Venus (Johnson & Baker 1994). Interestingly, few of the Venus outflows exhibit the very high CPR values of lunar examples, suggesting either some difference in emplacement conditions or more rapid erosion under Venus conditions. Recent Earth-based radar observations have also built on the lunar experience to map extensive fine-grained crater ejecta deposits in the tessera highlands of Venus (Campbell et al. 2015).

Of great importance to Venus and Mars volcanic and impact-crater studies is the relationship between surface roughness characteristics, fine-grained mantling deposits, and radar back-scatter properties. Earth-based radar maps of Mars with spatial resolution of about 3 km have been produced, and show a wide range of volcanic and ancient fluvial landforms that are often hidden from view by meters of dust (e.g., Harmon et al. 1999, 2012). Just how extremely rough some of the lava flows are, perhaps due to enhanced silica content, is demonstrated by a comparison of their CPR values to those of terrestrial lava flows, from which only the most blocky or platy appear to provide adequate analogs (Harmon et al. 1999). For Venus, the range of brightness and CPR values in Earth-based data can link flows seen only by radar to those observed on Earth (Plaut 1991; Campbell & Campbell 1992), and polarimetric analysis identifies where the plains are mantled by fine-grained sediments (Carter et al. 2004, 2006). The lunar work, where we can compare the radar depth of penetration to regolith composition, plays a major role in better constraining estimates of subsurface probing in planning for future Mars and Venus investigations.

Radar has been long used to study main belt and near-Earth asteroids (e.g., Ostro et al. 1985), with a particular recent emphasis on the physical shape and density structure of objects that may pose a risk of impact. For many of the distant asteroids, physical analysis is limited to their overall radar cross section and polarization ratios (Shepard et al. 2010), and to date there has been limited opportunity to apply the polarimetric imaging applications used in geologic work for the Moon, Mars, Venus, or Mercury. These techniques might well, however, find application in orbital radar studies of potentially ice-rich dwarf planets like Ceres. The outer planet satellites have likewise been studied by radar with moderate spatial resolution, and there are clearly variations in scattering properties across their surfaces that may indicate differences in the age, degree of modification, or composition of the materials (Ostro et al. 1992). Only Titan has been visited by an orbital imaging radar system, and the Cassini mission has provided a striking view of mountains, lakes, dunes, and cryovolcanism on this enigmatic world. With a single polarization, the Cassini radar data do not allow for polarimetric analysis, but the low microwave losses within many low-temperature ices and hydrocarbon liquids have generated interesting questions about the role of surface and subsurface scattering across Titan (e.g., Mastrogiuseppe et al. 2014) that may gain from the inner-planet studies.

In closing, we can look at the state of the field and expectations for the future. Earth-based radar investigations at longer wavelengths (12.6 and 70 cm) depend on the continued operation of the transmitters in Arecibo, and lunar work for these frequencies must also have a receiving system such as the GBT. Ongoing work uses the highest resolutions possible to address specific lunar science problems, such as the details of mare unit stratigraphy or the occurrence of small pyroclastic deposits. Mapping of Venus (Figure 20) was carried out during the inferior conjunctions of 2012 (Campbell et al. 2015) and 2015, and represents the only way to make polarimetric studies and monitor the surface for evidence of volcanic events until a new orbital mission is selected. Studies of near-Earth objects represent a distinct and vibrant area of research for both the Arecibo-GBT combination and Goldstone. Long-term measurements of planetary motions using the speckle-displacement
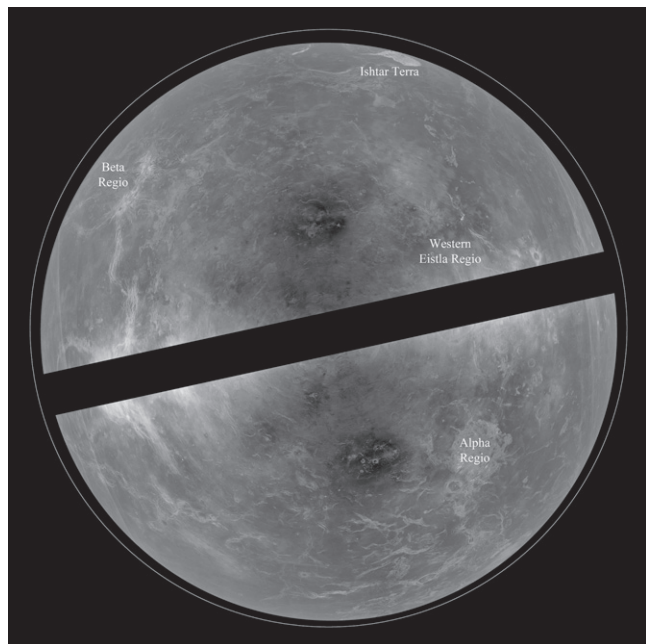
Figure 20. Radar image of Venus collected during the 2012 inferior conjunction using the Arecibo Observatory and Green Bank Telescope. Spatial resolution is about 1.5 km. Major landforms are labeled. The dark band at center represents areas where the Doppler-resolved image resolution is very coarse.

method continue to refine understanding of core properties on Mercury and Venus (Margot et al. 2007).

Radar sounders are planned for both U.S. and European missions to the Jovian icy satellites, building on the success of the Mars-orbiting MARSIS and SHARAD sensors in probing the ice caps and other landforms. A radar sounder surveyed the Moon as part of the Kaguya mission, and orbital imaging sensors at X-band (4.2 cm) and S-band (12.6 cm) have flown with the *Chandrayaan-1* and *LRO* missions (Nozette et al. 2010). The success of so many deep-probing studies with the Earth-based 70 cm system (Section 7) suggests that longer-wavelength orbital imaging radar could make significant new lunar discoveries.

At present, the potential for new imaging sensors on other orbital missions remains a topic of discussion, and of proposals to competitive NASA mission programs like Discovery and New Frontiers. For example, an orbital radar sensor at Venus could carry our understanding of the surface geology and geophysics far beyond that of *Magellan* by collecting high-resolution images, polarimetric information, detailed topography, and perhaps detecting active ground motion through interferometry (NASA Venus Flagship Mission Study 2009). A Mars-orbiting imaging radar could identify and map shallow ground ice, help to understand the seasonal occurrence of flow-

like surface features, and reveal the bedrock geology over vast areas mantled by dust (Campbell et al. 2004).

References

Black, G. J., Campbell, D. B., & Nicholson, P. D. 2001, Icar, 151, 167
Butrica, A. J. 1996, To See the Unseen (Washington: NASA History Office)
Campbell, B. A. 2001, Icar, 150, 38
Campbell, B. A. 2002, Radar Remote Sensing of Planetary Surfaces (New York: Cambridge Univ. Press)
Campbell, B. A. 2009, ITGRS, 47, 3480
Campbell, B. A. 2012, JGR, 117, E06008
Campbell, B. A., Arvidson, R. E., & Shepard, M. K. 1993, JGR, 98, 17099
Campbell, B. A., Bell, J. F., Hawke, B. R., & Horton, K. A. 1992, LPSC, 22, 259
Campbell, B. A., & Campbell, D. B. 1992, JGR, 97, 16293
Campbell, B. A., & Campbell, D. B. 2006, Icar, 180, 1
Campbell, B. A., Campbell, D. B., Chandler, J. F., et al. 2003, Natur, 426, 137
Campbell, B. A., Campbell, D. B., Margot, J. L., et al. 2007, ITGRS, 45, 4032
Campbell, B. A., Campbell, D. B., Morgan, G. A., et al. 2015, Icar, 250, 123
Campbell, B. A., Carter, L. M., Campbell, D. B., et al. 2010, Icar, 208, 565
Campbell, B. A., Carter, L. M., Hawke, B. R., Campbell, D. B., & Ghent, R. R. 2008, Geo, 36, 135
Campbell, B. A., Freeman, A., Veilleux, L., et al. 2004, in Proc. IEEE Aerospace Conf., Vol. 1 (New York: IEEE), 503
Campbell, B. A., & Hawke, B. R. 2005, JGR, 110, E09002
Campbell, B. A., Hawke, B. R., & Campbell, D. B. 2009a, JGR, 114, E01001
Campbell, B. A., Hawke, B. R., Carter, L. M., Ghent, R. R., & Campbell, D. B. 2009b, GeoRL, 36, L22201
Campbell, B. A., Hawke, B. R., Morgan, G. A., et al. 2014, JGR, 119, 313
Campbell, B. A., Hawke, B. R., & Thompson, T. W. 1997, JGR, 102, 19307
Campbell, B. A., & Shepard, M. K. 1996, JGR, 101, 18941

Campbell, B. A., Zisk, S. H., & Mouginis-Mark, P. J. 1989, RSEnv, 30, 227

Campbell, D. B., Campbell, B. A., Carter, L. M., Margot, J. L., & Stacy, N. J. S. 2006, Natur, 443, 835

Campbell, D. B., Dyce, R. B., Ingalls, R. P., Pettengill, G. H., & Shapiro, I. I. 1972, Sci, 175, 514

Campbell, D. B., et al. 1989, Sci, 246, 373

Carrier, W. D., Olhoeft, G. R., & Mendell, W. 1991, Lunar Sourcebook (New York: Cambridge Univ. Press)

Carter, L. M., Campbell, B. A., Hawke, B. R., Campbell, D. B., & Nolan, M. C. 2009, JGR, 114, E11004

Carter, L. M., Campbell, D. B., & Campbell, B. A. 2004, JGR, 109, E06009

Carter, L. M., Campbell, D. B., & Campbell, B. A. 2006, JGR, 111, E06005

Carter, L. M., Campbell, D. B., & Campbell, B. A. 2011, Proc. IEEE, 99, 770

Carter, L. M., Neish, C. D., Bussey, D. B. J., et al. 2012, JGR, 117, E00H09

Cumming, I. G., & Wong, F. H. 2004, Digital Processing of Synthetic Aperture Radar Data; Algorithms and Implementation (Norwood, MA: Artech House)

Evans, D. L., Farr, T. G., Ford, J. P., Thompson, T. W., & Werner, C. L. 1986, ITGRS, GE-24, 246

Evans, J. V. 1968, in Radar Astronomy, ed. T. Hagfors, & J. V. Evans (New York: McGraw-Hill), 501

Feldman, W. C., et al. 2001, JGR, 106, 23232

Gaddis, L. R. 1992, GSAB, 104, 695

Gaddis, L. R., Pieters, C. M., & Hawke, B. R. 1985, Icar, 61, 461

Ghent, R. R., Campbell, B. A., Hawke, B. R., & Campbell, D. B. 2008, Geo, 36, 343

Ghent, R. R., Gupta, V., Campbell, B. A., et al. 2010, Icar, 209, 818

Ghent, R. R., Hayne, P. O., Bandfield, J. L., et al. 2014, Geo, 42, 1059

Ghent, R. R., Leverington, D. W., Campbell, B. A., Hawke, B. R., & Campbell, D. B. 2005, JGR, 110, E02005

Hagfors, T. 1964, JGR, 69, 3779

Hagfors, T. 1970, RaSc, 5, 189

Hagfors, T., & Evans, J. V. 1968, in Radar Astronomy (New York: McGraw-Hill), 251

Harmon, J. K., Arvidson, R. E., Guinness, E. A., Campbell, B. A., & Slade, M. A. 1999, JGR, 104, 14065

Harmon, J. K., Nolan, M. C., Husmann, D. I., & Campbell, B. A. 2012, Icar, 220, 990

Harmon, J. K., Slade, M. A., & Rice, M. S. 2011, Icar, 211, 37

Hawke, B. R., Blewett, D. T., Lucey, P. G., et al. 2004, Icar, 170, 1

Hawke, B. R., Coombs, C. R., Campbell, B. A., et al. 1990, LPSC, 21, 377

Hawke, B. R., Peterson, C. A., Lucey, P. G., et al. 1993, GeoRL, 20, 419

Hiesinger, H., Jaumann, R., Neukum, G., & Head, J. W. 2000, JGR, 105, 29239

Johnson, J. R., & Baker, V. R. 1994, Icar, 110, 33

Margot, J. L., Campbell, D. B., Jurgens, R. F., & Slade, M. A. 1999, Sci, 284, 1658

Margot, J. L., Campbell, D. B., Jurgens, R. F., & Slade, M. A. 2000, ITGRS, 38, 1122

Margot, J. L., Peale, S. J., Jurgens, R. F., Slade, M. A., & Holin, I. V. 2007, Sci, 316, 710

Mastrogiuseppe, M., Poggiali, V., Hayes, A., et al. 2014, GeoRL, 41, 1432

Mustard, J. F., & Head, J. W. 1996, JGR, 101, 18913

Neish, C. D., & Carter, L. M. 2014, Encyclopedia of the Solar System (Amsterdam: Elsevier)

Nozette, S., Spudis, P., Bussey, B., et al. 2010, SSRv, 150, 285

Nozette, S., Spudis, P. D., Robinson, M. S., et al. 2001, JGR, 106, 23253

Ostro, S. J. 1987, Encyclopedia of Physical Science and Technology (New York: Academic)

Ostro, S. J., Campbell, D. B., & Shapiro, I. I. 1985, Sci, 229, 442

Ostro, S. J., et al. 1992, JGR, 97, 18277

Pettengill, G. H., & Thompson, T. W. 1968, Icar, 8, 457

Plaut, J. J. 1991, PhD thesis, Washington Univ.

Raney, R. K. 2007, ITGRS, 45, 3397

Raney, R. K., Spudis, P. D., Bussey, D. B. J., et al. 2011, Proc. IEEE, 99, 808

Saunders, R. S., et al. 1992, JGR, 97, 13067

Schaber, G. G., Thompson, T. W., & Zisk, S. H. 1975, Moon, 13, 395

Schultz, P. H., & Spudis, P. D. 1979, LPSC, 10, 2899

Shepard, M. K., Brackett, R. A., & Arvidson, R. E. 1995, JGR, 100, 11709

Shepard, M. K., Campbell, B. A., Bulmer, M., et al. 2001, JGR, 106, 32777

Shepard, M. K., Clark, B. E., Ockert-Bell, M., et al. 2010, Icar, 208, 221

Shoemaker, E. M. 1971, Univ. de Barcelona, Vol. XXV, 26

Slade, M. A., Butler, B. J., & Muhleman, D. O. 1992, Sci, 258, 635

Spudis, P. D., Bussey, D. B. J., Baloga, S. M., et al. 2010, GeoRL, 37, L06204

Stacy, N. J. S. 1993, Ph.D. thesis, Ithaca, NY: Cornell Univ.

Stacy, N. J. S., & Campbell, D. B. 1993, in Proc. IEEE Int. Geoscience and Remote Sensing Symp., Vol. 1, (New York: IEEE), 30

Stacy, N. J. S., Campbell, D. B., & Ford, P. G. 1997, Sci, 276, 1527

Thompson, T. W. 1974, Moon, 10, 51

Thompson, T. W. 1987, EM&P, 37, 59

Thompson, T. W., Campbell, B. A., Ghent, R. R., Hawke, B. R., & Leverington, D. W. 2006, JGR, 111, E06S14

Thompson, T. W., & Dyce, R. B. 1966, JGR, 71, 4843

Thompson, T. W., Pollack, J. B., Campbell, M. J., & O'Leary, B. T. 1970, RaSc, 5, 253

Thompson, T. W., Roberts, W. J., Hartmann, W. K., Shorthill, R. W., & Zisk, S. H. 1979, M&P, 21, 319

van Zyl, J. J., Zebker, H. A., & Elachi, C. 1987, RaSc, 22, 529

Venus Flagship Mission Study: Report of the Venus Science and Technology Definition Team 2009, NASA

Wahl, D. E., Eichel, P. H., Ghiglia, D. C., & Jakowatz, C. V. 1984, ITAES, 30, 827

Wells, K. S., Campbell, D. B., Campbell, B. A., & Carter, L. M. 2010, JGR, 115, E06008

Wilcox, B. B., Robinson, M. S., Thomas, P. C., & Hawke, B. R. 2005, M&PS, 40, 695

Zisk, S. H., Campbell, B. A., Pettengill, G. H., & Brockelman, R. 1991, GeoRL, 18, 2137

Zisk, S. H., Pettengill, G. H., & Catuna, G. W. 1974, Moon, 10, 17

Zisk, S. H., et al. 1977, Moon, 17, 59